Available online at www.CivileJournal.org

Civil Engineering Journal

(E-ISSN: 2476-3055; ISSN: 2676-6957)

Vol. 11, No. 11, November, 2025

Fragility Assessment of Cable-Stayed Bridge Towers Under Scaled Earthquakes

Nouran Mamdouh [1*], Walid A. Attia [2], Mohamed S. Elbayomy [2]

[1] *Department of Structural Engineering, Cairo University, El Gazeera Engineering Institute (EGI), El Abageya–El Mokattam, Cairo, Egypt.*

[2] *Department of Structural Engineering, Faculty of Engineering, Cairo University, Giza, Egypt.*

Received 20 March 2025; Revised 21 October 2025; Accepted 27 October 2025; Published 01 November 2025

Abstract

Cable-stayed bridges exhibit exceptional vulnerability to seismic excitation, particularly under combined vertical and horizontal ground motions in tectonically active regions. This study characterizes the seismic fragility of cable-stayed bridge towers using comprehensive probabilistic assessment methodologies. The framework integrates fragility curve development and Monte Carlo simulation, employing 30 earthquake ground motion records to construct robust statistical models of structural response. Fragility functions quantify the probability of exceeding predefined damage states across varying seismic intensity measures, while Monte Carlo analyses capture the stochastic nature of behavior and highlight response clustering around mean performance levels for distinct classifications. The findings reveal pronounced structural vulnerabilities within cable-stayed bridge systems, shaped by both epistemic and aleatory uncertainties that may lead to progressive collapse under extreme seismic events. Computational results indicate that although responses converge statistically around expected values, considerable scatter persists across limit states. For instance, at Sa(T1) = 1.0 g, exceedance probabilities diverge significantly: OP is almost certain (>99.9%), IO reaches 86.5%, DC 46.9%, and CP only 10.9%. Under more severe shaking (2.0 g), DC exceedance exceeds 98%, while CP remains 31%, illustrating substantial variability in fragility across thresholds. These results underscore the urgent need for improved seismic design philosophies in cable-stayed infrastructure within hazardous environments. The research advances bridge engineering practice by clarifying fundamental vulnerability mechanisms and guiding the development of innovative material systems, retrofit strategies, and structural health monitoring protocols aimed at enhancing seismic resilience.

Keywords: Cable-Stayed Bridges; Seismic Fragility Analysis; Monte Carlo Simulation; Ground Motion Records; Damage States; Uncertainty Quantification.

1. Introduction

Bridges represent essential components of modern infrastructure, supporting both economic growth and social connectivity. Among them, cable-stayed bridges have become the preferred solution for medium to long spans (200–1000 m), due to their superior structural efficiency and architectural appeal. Their distinctive configuration, defined by direct cable connections between towers and deck, allows for effective load distribution but also introduces complex seismic behavior arising from coupled deck–tower–cable interactions. Consequently, seismic vulnerability assessment of cable-stayed bridges has received growing attention, especially after major earthquakes highlighted the risks faced by critical infrastructure. Early pioneering works [1, 2] laid the foundation for seismic analysis of such systems through three-dimensional nonlinear modelling that incorporated cable sag, axial–bending interactions, and geometric

* Corresponding author: nouran.nagdy.s@eng-st.cu.edu.eg

http://dx.doi.org/10.28991/CEJ-2025-011-11-011

nonlinearities under both uniform and multi-support excitations. These investigations revealed that cable-stayed bridges exhibit unique dynamic behavior under seismic loading, requiring dedicated analytical frameworks.

The literature further advanced with the development of fragility curves as a probabilistic tool to quantify vulnerability. The seminal work of Shinozuka et al. [3] introduced a systematic method to relate structural damage probabilities to seismic intensity measures, and this methodology was enhanced by subsequent studies [4] that applied Monte Carlo simulation to incorporate uncertainty quantification. Building upon these foundations, later research [5–7] developed refined nonlinear finite element models to generate both component-level and system-level fragility curves, showing the vulnerability of expansion joints, deck–pier connections, and cables. More recent contributions considered multi-hazard interactions, particularly the combined impact of seismic and wind loads, which demonstrated the limitations of single-hazard evaluations [7]. In addition, specialized studies addressed sea-crossing cable-stayed bridges by integrating multi-support ground motion and soil–structure interaction [8], fault-crossing scenarios with near-fault ground motions [9], and the implications of cable loss under seismic loading [10].

Despite these advances, several research gaps remain. Many fragility analyses still rely on simplified models that do not capture the full nonlinear behavior of cable-stayed bridges [11], while uncertainty quantification is often partial, neglecting the combined epistemic and aleatory uncertainties that influence reliability assessments [12]. The effects of soil–structure interaction on tower foundations have not been sufficiently incorporated [8], and region-specific analyses are largely missing, particularly in the Middle East and North Africa, despite the region's significant seismic exposure [13]. Furthermore, many studies continue to use limited suites of ground motions that fail to represent regional hazard characteristics [14], raising concerns about the practical accuracy of their fragility predictions.

The present research seeks to address these gaps by developing a comprehensive framework for seismic fragility assessment of cable-stayed bridges. Following the structure of the study, Section 2 then outlines the methods for developing fragility curves, with emphasis on lognormal probabilistic formulations and intensity measure selection. Section 3 presents the overall methodology, describing the analytical workflow that integrates nonlinear finite element modelling, pushover analysis, and probabilistic assessment. Section 4 introduces the selected case study bridge, with full details of its geometry, material properties, and numerical modelling strategy. Section 5 explains the process of selecting thirty ground motion records that capture the regional seismic hazard, while Section 6 describes the scaling methodology applied to ensure spectral compatibility. Section 7 discusses the pushover analysis carried out to evaluate structural performance and identify capacity points, which then feed into Section 8, where fragility analysis is performed to establish probability of exceedance curves. Section 9 introduces the Monte Carlo approach as a tool to incorporate uncertainty systematically into the fragility framework. Section 10 presents the discussion, linking the results of the fragility curves with the broader literature and highlighting the implications for vulnerability assessment. Finally, Section 11 concludes the study, summarizing the key findings and offering recommendations for practical applications and future research.

In discussion, the results of the present fragility analysis are consistent with earlier findings [5–7], which highlighted the vulnerability of expansion joints, cables, and deck–pier connections as critical components influencing system-level fragility. However, by explicitly incorporating regional seismic hazard data and a wider ground motion database, this study extends previous approaches and provides more context-specific vulnerability predictions. Compared to specialized studies on sea-crossing bridges [8] or near-fault conditions [9], the current framework demonstrates broader applicability, especially in addressing uncertainties using Monte Carlo simulations. Furthermore, the integration of soil–structure interaction effects add realism often overlooked in prior models. These contributions position the research as a significant step forward, aligning with the performance-based design philosophy while offering practical tools for retrofit prioritization.

Through this framework, the study integrates advanced nonlinear finite element modelling with probabilistic techniques to overcome current limitations. By explicitly accounting for large-displacement behavior, material nonlinearities, and cable sag, the research delivers a more realistic representation of structural performance. Furthermore, by employing Monte Carlo simulations and a carefully selected regional ground motion database, the study enhances the robustness and applicability of fragility predictions. The resulting fragility curves not only contribute to theoretical advancements but also offer practical tools for seismic risk assessment, retrofit prioritization, and performance-based design of cable-stayed bridges. In doing so, this research provides a significant step toward improving the seismic resilience of critical bridge infrastructure in earthquake-prone regions.

2. Methods for Developing Fragility Curves

Researchers have employed various techniques to develop fragility curves, which are essential for assessing the vulnerability of structures to seismic events. These methods include expert-based, empirical, experimental, analytical, and hybrid approaches [15]. Each method offers distinct advantages and faces specific limitations. Expert-based fragility curves are some of the earliest and simplest methods for developing fragility functions, relying on the opinions of earthquake engineering experts to estimate potential damage to bridge components under varying earthquake intensities.

These expert judgments are used to construct probability distribution functions that represent the likelihood of reaching specific damage levels at different seismic intensities. However, this method is highly subjective and prone to bias due to factors such as the design of the questionnaire, the composition and experience of the expert panel, and the overall approach, leading to considerable uncertainties [16].

Empirical fragility curves, derived from observed damage distributions following real earthquakes, provide a more realistic representation of vulnerability but are also subject to significant uncertainty due to inconsistencies in damage observations by different inspection teams [17]. For example, studies by Abdel-Ghaffar & Nazmy [2] and Shinozuka et al. [18] on the 1995 Kobe earthquake produced significantly different empirical fragility curves, illustrating the variability inherent in this approach.

Experimental fragility curves, though less common due to the high costs of large-scale experiments, offer valuable insights into the actual performance of bridge components under seismic loads. These curves are typically developed using data from tests such as shake table or cyclic load tests, providing a probabilistic relationship between experimental damage data and seismic response parameters [19]. Fragility functions quantify the probability of a structure exceeding specific damage levels given a certain level of ground shaking. These functions relate earthquake intensity to the likelihood of reaching or surpassing particular damage thresholds. Vulnerability functions can be derived from fragility functions by incorporating the expected consequences or losses associated with various damage states resulting from seismic events [20].

2.1. The Approach of Fragility Curves

In fragility analysis, various mathematical distribution functions can be used to estimate the probability of exceeding these damage states. The uniform, lognormal, and normal distributions are the most commonly utilized distribution types. Because of these distributions' distinct properties, each one is suitable for a specific set of applications.

- Normal Distribution: Due to its ease of calculation and understanding, the symmetrical is widely employed in computations. However, occasionally, particularly in the case of extreme events where damage is likely to occur, it might not accurately reflect the skewed character of seismic data [15].
- Lognormal Distribution: The lognormal distribution is skewed at Equation 1, in contrast to the normal distribution, which allows it to more precisely represent the likelihood of uncommon, highly significant events. Because of this skewness, it is especially helpful in seismic fragility analyses, where increased seismic intensities are associated with a fast-increasing probability of serious damage. Since smaller seismic events are far more common than larger, more destructive ones and because it offers a more realistic assessment of seismic hazard exceedance and associated risks, the lognormal distribution is preferred in many cases [16].

Uniform distributions, which assume that all possible outcomes within a specific range have an equal probability, are less commonly used in fragility analysis because they do not accurately represent the distribution of seismic occurrences and their effects. Instead, researchers often rely on the cumulative distribution function (CDF) of more suitable distributions to assess the probability that a given level of ground motion will result in a certain level of damage. The CDF is essentially a plot that shows the cumulative probability of not exceeding a particular damage state as the intensity of ground motion increases.

$$P(LS/IM) = \Phi\left(\frac{\ln(\mathrm{IM})-\lambda}{\varsigma}\right) \quad (1)$$

The standard equation for developing fragility curves or conditional exceedance is represented as:

where Φ[.] is the cumulative distribution function, IM stands for Intensity Measure, and it refers to the level or strength of seismic ground motion experienced during an earthquake. It is a key variable in seismic analysis and fragility curves because it quantifies the severity of the earthquake shaking at a specific location, **λ** is the median value of the fragility function, and **ζ** is the standard deviation of the natural logarithm of IM.

In this equation, LS refers to limit states or damage states, and the term **y** to represent the damage state reached by the structure in response to a given intensity of ground motion (IM). Conceptually, **y** refers to the specific outcome or level of damage that the structure experiences as a result of the seismic event. While not explicitly included in the mathematical formulation of the fragility curve, **y** provides a useful framework for understanding the relationship between ground motion intensity and the resultant damage.

These fragility curves are designed to predict hazard risk during and after seismic events and are commonly used to mitigate damage and energy loss during earthquakes. They also serve as a foundation for building codes in specific regions. These fragility curves are designed to predict hazard risk during and after seismic events, and are commonly used to mitigate damage and energy loss during earthquakes, providing a basis for building codes in specific regions [21].

3. Research Methodology

The adopted methodology for developing seismic fragility curves is presented in the flowchart "Procedure for Deriving Fragility Curves and Monte Carlo Evaluation" (Figure 1). Initially, a structural model was established by defining geometry, material properties, mass, damping, and boundary conditions. A nonlinear pushover analysis was then conducted to obtain the base shear–roof displacement curve, which was transformed into the Acceleration–Displacement Response Spectrum (Sa–Sd). Structural limit states were defined and mapped onto the capacity curve, after which the performance point was determined and engineering demand parameters (e.g., roof drift) were computed. Fragility functions were subsequently developed to quantify exceedance probabilities of different damage states. Finally, fragility curves and histograms were generated, and a Monte Carlo simulation with varying sample sizes (100, 1,000, and 10,000) was performed to evaluate the uncertainty and robustness of the results.

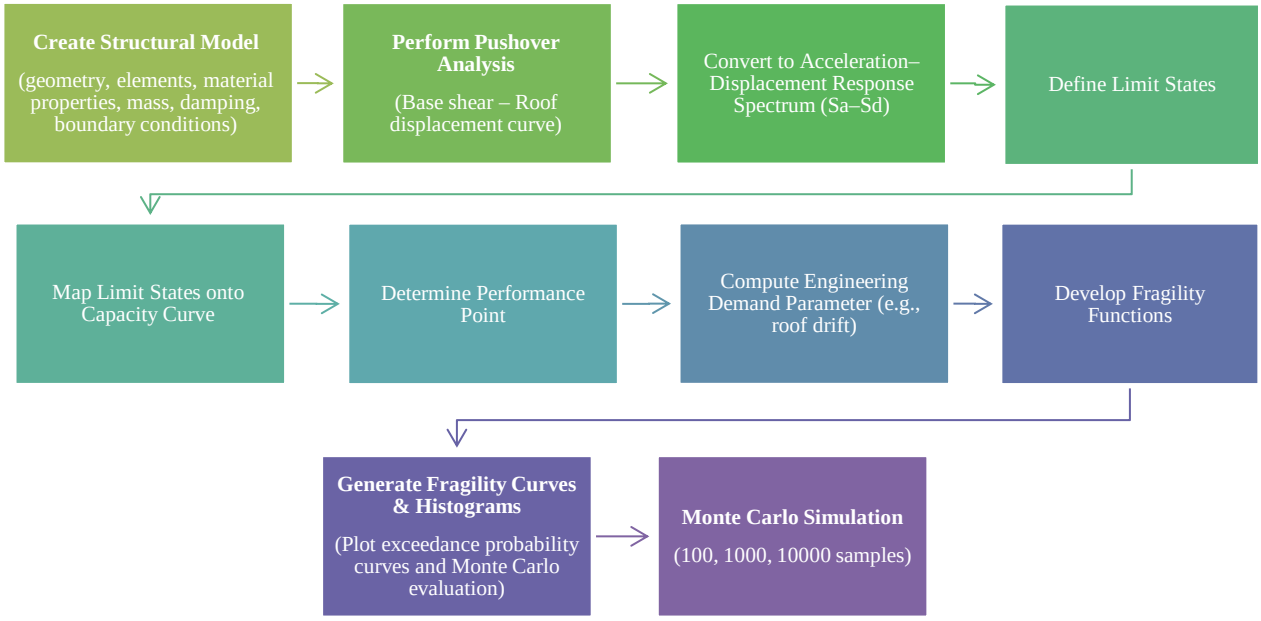

Figure 1. Procedure for Developing Seismic Fragility Curves and Monte Carlo Evaluation

4. Description of Selected Model

4.1. Description

The Peace Bridge was selected not only for its considerable dimensions spanning a total of 4,100 m the bridge is composed of three main sections:

The central section is a cable-stayed bridge that measures 730 meters in length and 20.80 meters in width. It includes a central span of 404 meters that crosses the Suez Canal, flanked by two side spans of 163 meters each. The approach bridges are positioned on the eastern and western sides of the canal and are constructed using concrete girders with a box-section design [22], but also because it represents a broader class of modern long-span cable-stayed bridges in Egypt. Its strategic location across the Suez Canal and its advanced structural system makes it a representative case for evaluating seismic vulnerability and fragility characteristics of critical national infrastructure. Consequently, the insights derived from this case study can be extended to inform the seismic assessment and resilience planning of similar bridges within Egypt and other earthquake-prone regions.

Recognized as the tallest cable-stayed bridge globally, the Peace Bridge offers a clearance of approximately 70 meters above the Suez Canal. The main section of the bridge has been designed with a vertical slope of 3.3% to ensure smooth traffic flow and a horizontal slope of 2% to facilitate effective drainage. The structure is supported by 128 stay cables. The design of the bridge was a collaborative effort between Pacific Consultants International and Chodai Co., Ltd. from Japan, in conjunction with Arab Consulting Engineers from Egypt. The construction was carried out by a Japanese consortium, which included Kajima, NKK, and Nippon Steel for the cable-stayed portion, while the General Nile Company for Roads and Bridges and Arab Contractors were responsible for the concrete approach spans. The project was managed under the oversight of the Egyptian General Authority for Roads, Bridges, and Land Transport (GARBLT).

The steel girder used in the main bridge has a box-type cross-section, with a maximum depth of 2.60 meters and a width of 20.80 meters, extending over a length of 730 meters and weighing 7,400 tons. The reinforced concrete pylons are H-shaped and reach a height of 154 meters, with a crossbeam located at 124.40 meters above the ground. Each pylon is assumed to have a fixed support at its base.

The stay cables are made up of parallel galvanized wire strands provided by Nippon Steel in Japan. These cables are arranged in a semi-fan configuration, with 4x16 cables in each plane, spaced 10 meters apart for the side spans and 20 meters apart for the main span. The cables terminate in NS-Sockets developed by Nippon Steel, which include a hot-poured zinc-copper alloy cone with epoxy resin to prevent fretting corrosion and reduce stress concentration.

In this study, they allow rotational movement while restricting any translational movement. This simplification helps eliminate the complexities associated with soil–structure interaction, enabling the focus to remain on the bridge's structural behavior. The fixed supports at the pylons provide a stable foundation for the overall structure, while the hinged end supports offer rotational flexibility, allowing the bridge to adapt to loads without compromising its integrity. This approach streamlines the analysis, making it easier to simulate the bridge's dynamic response to seismic forces while maintaining an accurate representation of the towers' and girders' behavior [22]. Soil–structure interaction is intentionally excluded in this study, as the aim is to focus solely on the superstructure's behavior. While the potential influence of soil flexibility is acknowledged, it lies beyond the scope of the present work and may be addressed in future studies.

4.2. Model

The bridges are discretized using a three-dimensional finite element method, incorporating three types of elements at Figure 2 and Table 1: frame, shell, and cable. The bridge decks are represented as shell elements, while the towers and pylons are modelled using three-dimensional frame elements. Each node in these shell and frame elements has six degrees of freedom, allowing movement in the X, Y, and Z directions, along with rotation around these axes. The stayed cables are treated as tension-only elements, meaning they do not provide stiffness under compressive forces.

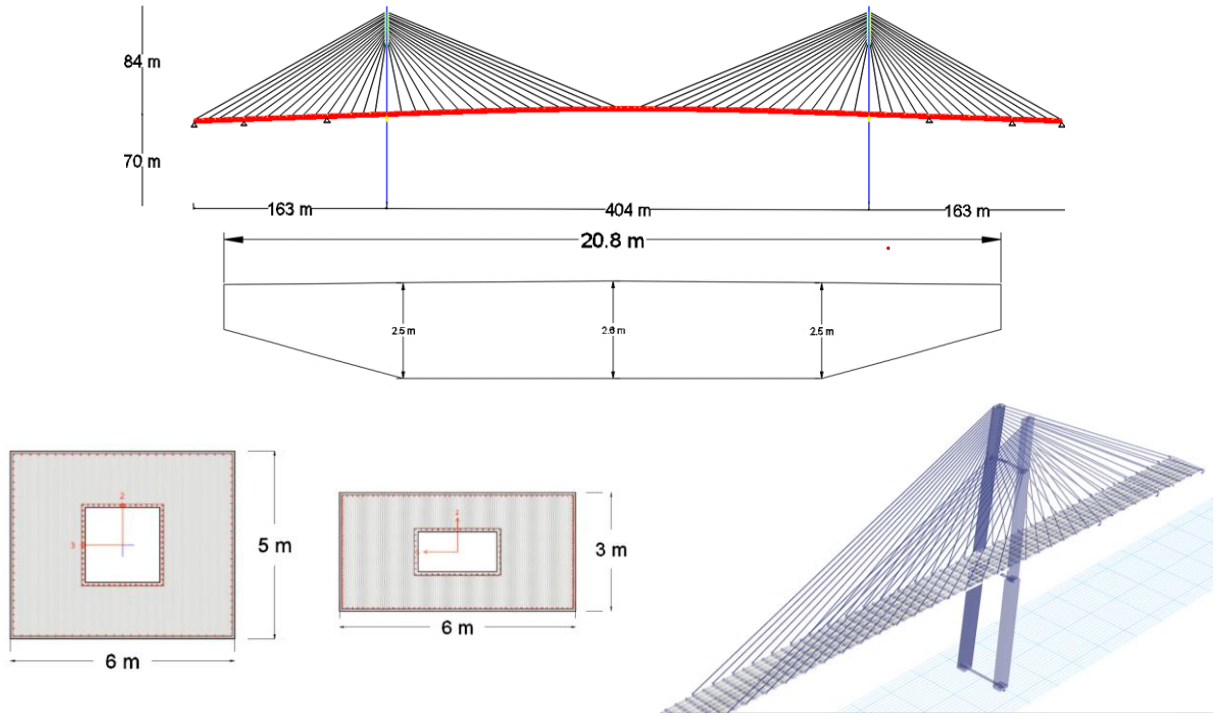

Figure 2. Model of the Cable-Stayed Bridge

Table 1. Structural members and their properties

S. N.	Structural Member	Dimension	Material	Shape
1	Cable	0.075 m Diameter	Steel	Circular
2	Deck	Width = 20.8 m, Depth = 2.6 m	Steel	Box Girder
3	Pylon Top	(2.0 m × 1.0 m)	RCC	Rectangular Box
4	Pylon Bottom	(6.0 m × 5.0 m), (2.0 m × 2.0 m)	RCC	Hollow Rectangular Box

In this analysis, Sap2000 v20 was utilized to model and assess the Peace Bridge with a high degree of precision. The bridge deck was represented using 8,756 shell elements, effectively simulating the complex configuration of the steel girder. The bridge's cables were modelled with 128 cable elements that included the effects of prestressing forces to accurately capture their structural behavior. To represent the pylons, four frame elements with variable

cross-sections were employed, allowing for an accurate depiction of their geometric intricacies, like as Figure 2. Nonlinear properties were integrated into these sections to reflect the realistic behavior of steel reinforcement and concrete under seismic loading conditions. The girder is represented by applying a gravity load of 8.5 kN/m² on the shell elements.

The bridge's columns are modelled as hinges, allowing for rotational movement while restricting translational displacement, as soil conditions are not included in this analysis. This approach simplifies the study by focusing solely on the structural behavior of the bridge, without the complexities introduced by soil-structure interaction. The fixed supports at the pylons provide a stable base for the entire structure, while the hinged columns offer rotational flexibility, enabling the bridge to respond to applied loads without compromising its stability. This method streamlines the simulation of the bridge's seismic response, ensuring a precise representation of the dynamic behavior of the towers and girders. For the time-history response analyses, a damping ratio of 2% was applied, consistent with standard practice for long-span bridges and the recommendations of Abdel-Ghaffar & Nazmy [2]. Alternative damping values were not explicitly tested, as the primary objective was to maintain alignment with established research and design guidelines. It is, however, acknowledged that the assumed damping ratio affects the fragility curves, where lower values would increase vulnerability while higher values would reduce it; thus, a detailed sensitivity study on damping effects is recommended for future work.

To realistically simulate the lateral restraint provided by wind shoe bearings, two horizontal rigid links with a 10 mm gap were incorporated between the bridge deck and the pylons. These elements are crucial for ensuring lateral stability and maintaining proper deck alignment under side forces such as wind, thereby enhancing the overall resistance of the bridge to lateral loads and improving its structural performance during dynamic excitations. To simulate the lateral support provided by wind shoe bearings, two horizontal rigid links with a 10 mm gap were installed between the bridge deck and the pylons. These simulated wind shoe bearings are essential for offering lateral stability, maintaining the proper alignment of the bridge deck under side forces such as wind. Including these components ensures the bridge can effectively resist lateral loads, thereby improving its structural strength and performance during dynamic loading conditions.

During the reinforcement detailing phase, the confinement effect on the concrete section was taken into consideration when modelling the behavior of both confined and unconfined concrete using a non-linear confinement model. Following AASHTO rules, the post-yield hardening ratio was established and used to quantify kinematic hardening based on yield forces and the member's initial stiffness. With a general force-type link, the bridge supports were treated as non-linearly, and the remainder of the structure was modelled as linearly elastic. As the linear analysis was carried out using modal superposition, the boundary conditions were studied by transforming the member forces from the non-linear system into equivalent loads within the linear system. With three translational and three rotational degrees of deformation allowed, the pylon support was represented as fixed.

To accurately represent the materials used in the bridge, concrete is assigned a modulus of elasticity (E) of 27.5 GPa, a Poisson's ratio (υ) of 0.2, and a mass density of 23.2 kN/m³. For steel, the modulus of elasticity (E) is 200 GPa, with a Poisson's ratio of 0.3 and a mass density of 78.6 kN/m³. Both materials are modelled as having linearly elastic behavior, with the same modulus of elasticity for both tension and compression . Additionally, a damping ratio of 2% is applied throughout the model, which is typical for bridges of this type, as noted by Abdel-Ghaffar & Nazmy [2].

5. Selection of Ground Motion

The procedure of choosing seismic recordings for a study such as the Suez Canal Cable-Stayed Bridge entails making sure the records selected correspond to the region's seismic hazard. To do this, choose or modify the data that match the local seismic design spectrum using the conditional spectrum approach. A wide range of seismic demands are recorded by selecting records from distinct seismic occurrences, such as the Chi-Chi and Northridge earthquakes, as shown in Table 2 which offer a variety of earthquake behaviors [23].

In order to meet the unique seismic circumstances of the area, the data are further modified using programs like SeismoMatch, which take into consideration variables like magnitude, source-to-site distance, and soil conditions. To provide a thorough study that simulates several possible seismic conditions, multiple recordings are used. The objective is to make sure the bridge is safe and resilient by using these recordings to fully assess the structure's performance under actual earthquake circumstances [24].

The ground motions' time history shows how the acceleration, expressed in "g" units, varies during the course of an earthquake. Each line in the graph indicates a ground motion record or an acceleration record from a particular seismic station, providing information about the duration and intensity of the earthquake. While the vertical axis depicts acceleration, the horizontal axis shows time in seconds (in Figure 3). The heaviest shaking is shown by peaks in the graph's early sections, whereas the later sections gradually diminish as the energy dissipates.

Table 2. Chosen Ground Motions Used as Bridge Excitation Inputs

No.	Event	Richter Scale	Location	Station
1	Northridge Earthquake	6.7	Wadsworth VA	USGS Station 235
2	Whittier Earthquake	5.9	Arcadia-Campus Dr.	USC Station 90093
3	Loma Prieta Earthquake	6.9	Anderson Dam L Abut	USGS Station 1652
4	Westmoreland Earthquake		Brawley Airport	USGS Station 5060
5	Northridge Earthquake	6.7	Century City LACC North	CDMG Station 24389
6	Chi-Chi Aftershock	7.6	CHY025 N	CWB (Central Weather Bureau)
7	Chi-Chi Aftershock	7.6	CHY029 N	CWB
8	Chi-Chi Aftershock	7.6	CHY036 N	CWB
9	Chi-Chi Aftershock	7.6	CHY080 N	CWB
10	Chi-Chi Aftershock	7.6	CHY046 N	CWB
11	Coalinga Earthquake	6.7	Pleasant Valley Pump FF	USBR Station 1162
12	Erzikan Earthquake	6.7	Erzikan North-South Comp	Erzikan
13	Loma Prieta Earthquake	6.9	Gilroy Array #4	CDMG Station 57382
14	Imperial Valley Earthquake	6.4	El Centro Array #5	USGS Station 952
15	Imperial Valley Earthquake	6.4	El Centro Array #12	USGS Station 931
16	Imperial Valley Earthquake	6.4	El Centro Diff Array	USGS Station 5165
17	Chi-Chi Aftershock	7.6	HWA011 E	CWB
18	Chi-Chi Aftershock	7.6	HWA013 E	CWB
19	Landers Earthquake	7.3	Indio-Coachella Canal	CDMG Station 12026
20	Northridge Earthquake	6.7	Jensen FLT PLT	Gen 22
21	Landers Earthquake	7.3	Lucerne	SCE Station 24
22	Northridge Earthquake	6.7	LA Dam	USGS Station 00000
23	Cape Mendocino Earthquake	7.2	Petrolia	CDMG Station 89156
24	Landers Earthquake	7.3	Pomona-4th & Locust	CDMG Station 23525
25	San Fernando Earthquake	6.6	Pacoima Dam	CDMG Station 164
26	Northridge Earthquake	6.7	Sylmar-Converter Sta-East	USGS Station 270
27	Chi-Chi Aftershock	7.6	TAP007 S	CWB
28	Chi-Chi Aftershock	7.6	TCU089 E	CWB
29	Chi-Chi Aftershock	7.6	TCU112 E	CWB
30	Chi-Chi Aftershock	7.6	TCU141 N	CWB

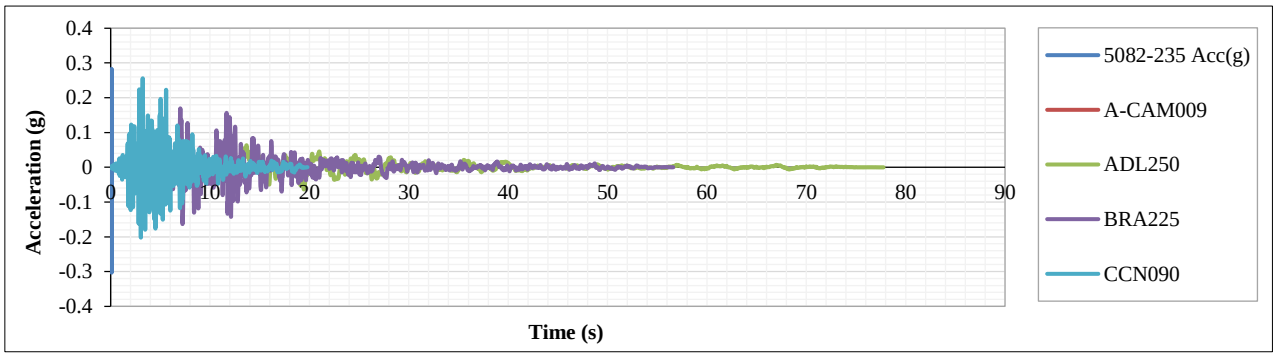

a) Acceleration Time History Records of First Five Ground Motions from Strong Motion Database

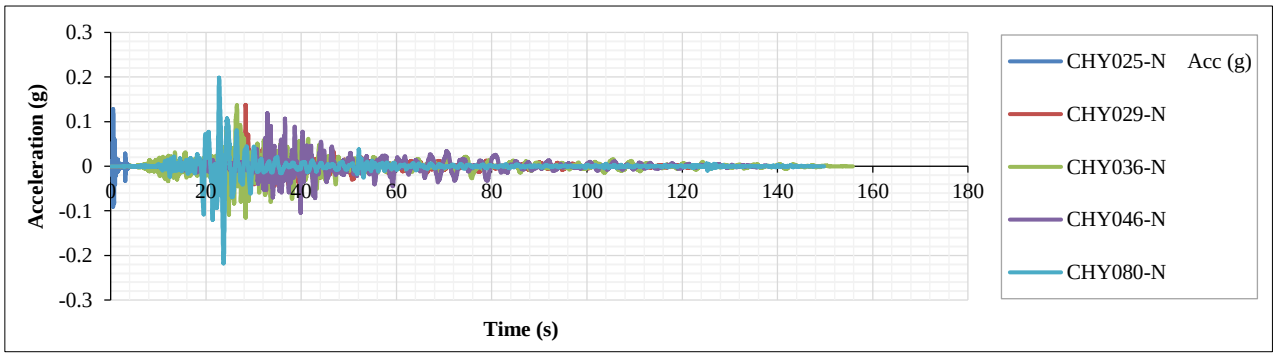

b) Acceleration Time History Records of Ground Motions 6-10 from Strong Motion Database

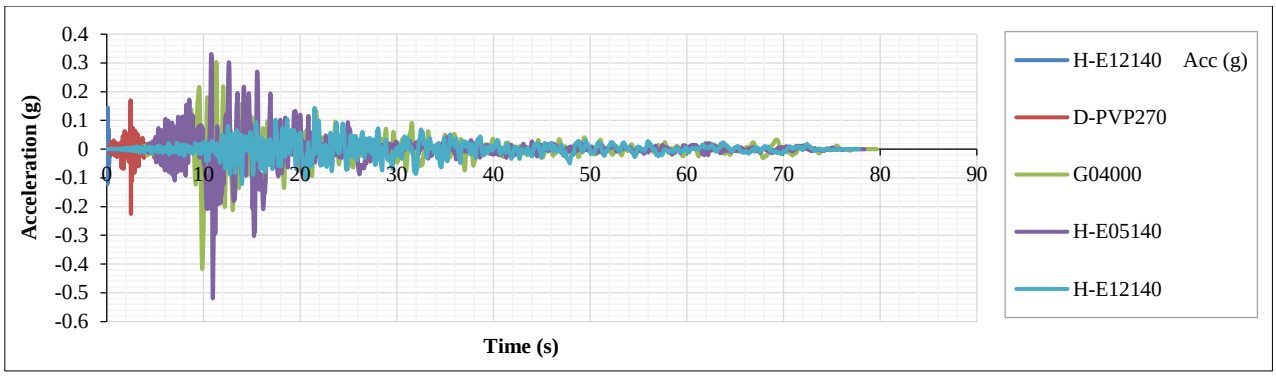

c) Acceleration Time History Records of Ground Motions 11-15 from Strong Motion Database

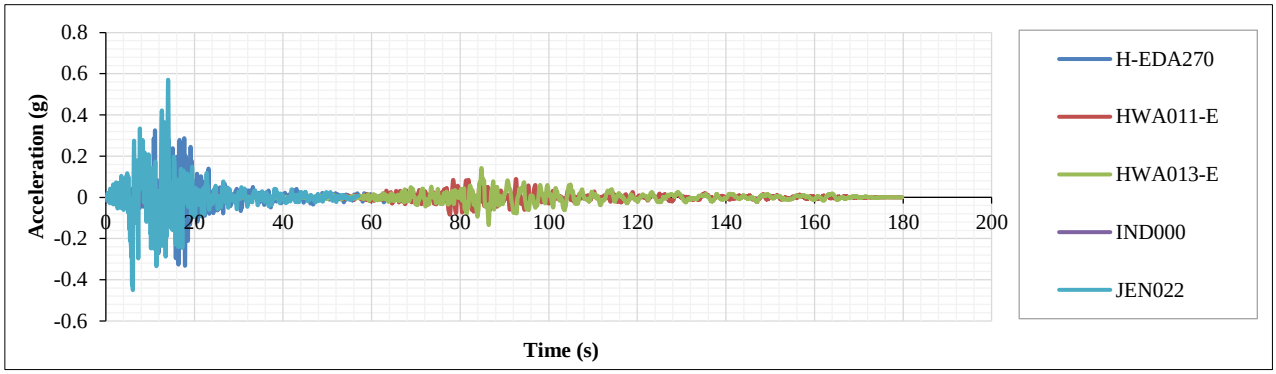

d) Acceleration Time History Records of Ground Motions 16-20 from Strong Motion Database

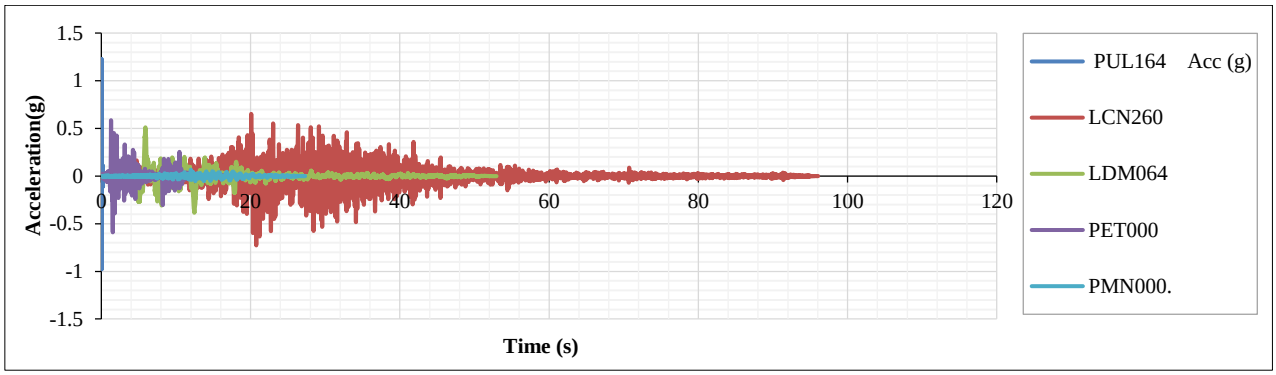

e) Acceleration Time History Records of Ground Motions 21-25 from Strong Motion Database

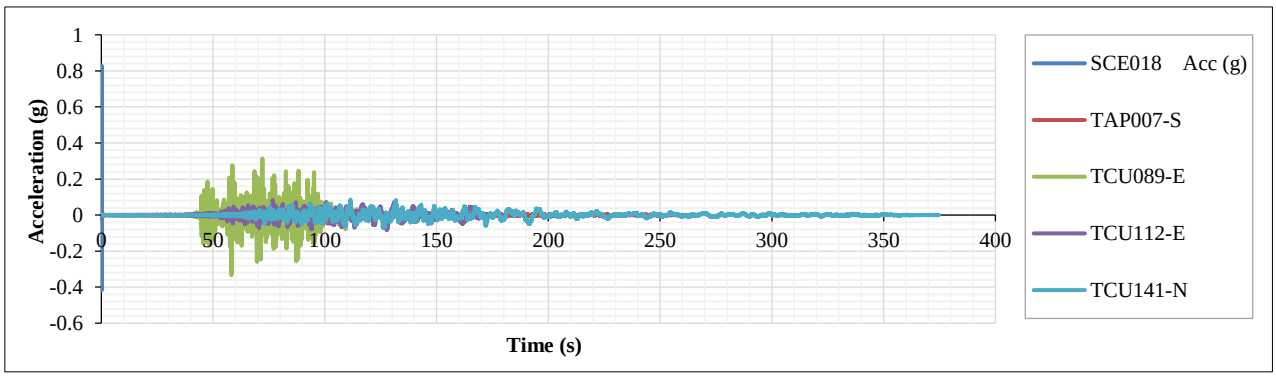

f) Acceleration Time History Records of Ground Motions 26-30 from Strong Motion Database

Figure 3. (a-f): Earthquake Records for Dynamic Analysis of the Suez Canal Bridge Tower

The response spectrums generated by SeismoMatch. SeismoMatch changes the frequency content of the original time history data once they are entered into the software to fit a predetermined target response spectrum. The vertical axis in these graphs displays spectral acceleration (Sa), which is the peak acceleration experienced by structures with varied natural periodicity (in Figure 4). The horizontal axis represents the period (T), which is the structure's natural period in seconds. Each line depicts a ground motion record's response spectrum after being changed to match the target spectrum.

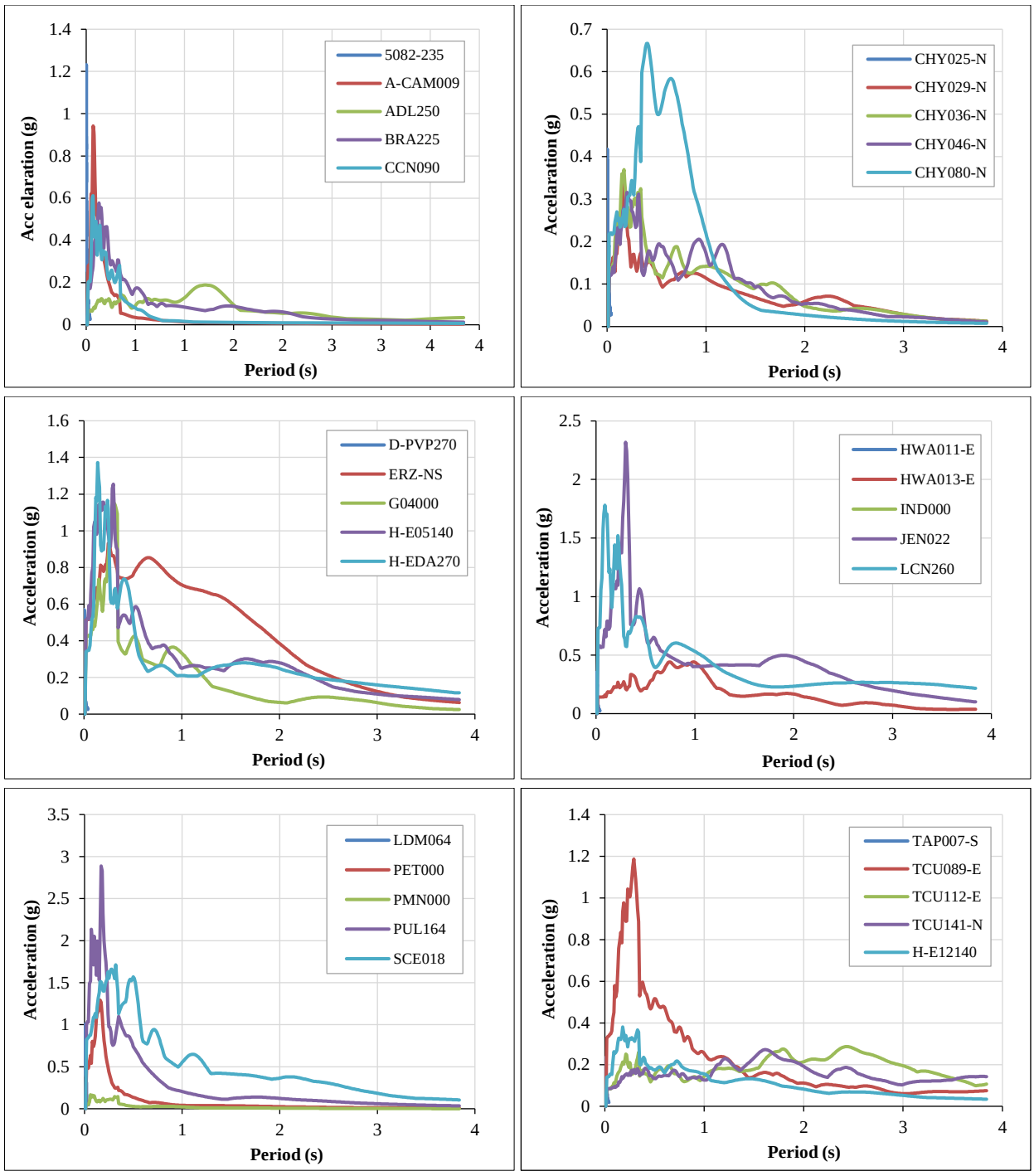

Figure 4. Response spectrum for 30 records of time history

The response spectra of the selected ground motions (Figure 4) show peak accelerations mainly at short periods (T < 1.0 s), with values decreasing as the period increases. Some records, such as BRA225 and HWA013-E, exhibit higher amplitudes, reflecting variability in energy content. Overall, the spectra capture a broad range of seismic demands relevant to the fundamental period of the Peace Bridge.

6. Scaling of Ground Motion

The target spectrum for seismic analysis in this context is defined according to Egyptian code for loads ECP-201(2012) [10], which provide detailed criteria for determining the seismic load pattern. In this specific analysis, the ground acceleration, represented by a_g is set at 0.15g, which corresponds to the expected intensity of ground motion for the site for zone 3 at map Figure 5 and from Table 3. The spectrum type is chosen as Type 2, tailored to the specific seismic conditions of the region, and the ground type is classified as Type B, indicating a stiff soil profile that affects how seismic waves propagate through the ground. A soil factor S of 1.35 is applied to adjust the base acceleration, reflecting the influence of the soil's stiffness on the seismic forces. The design response spectrum is further shaped by

the periods T_b, T_c and T_d, set at 0.05, 0.25, and 1.2 seconds, respectively by using Equation 4. These periods define the segments of the response spectrum curve, representing how the structure responds to different frequencies of ground motion [24]. The behavior factor q, which accounts for the structure's ductility and ability to dissipate energy, is set at 3, aligning with the requirements for the elastic response spectrum, also characterized by a behavior factor q_a of 3.

Table 3. Seismic Effect Zones for Selected Egyptian Cities (Cairo, Giza, North Sinai, South Sinai: Table (8-2-B) as per ECP 201-2012 [10])

Governorate	City	Zone
Cairo	All City	3
Giza	All City	3
North Sinai	Arish	3
North Sinai	Rafah	4
North Sinai	Bir al-Abd	2
South Sinai	Abu Redis	3
South Sinai	Sharm El-Sheikh	4
South Sinai	Dahab, Nuweiba, Taba	5

Note: Peace Bridge (El Salam Bridge) is sometimes considered in Zone 3 due to its extension into North Sinai, although administratively it lies in Ismailia (Zone 2).

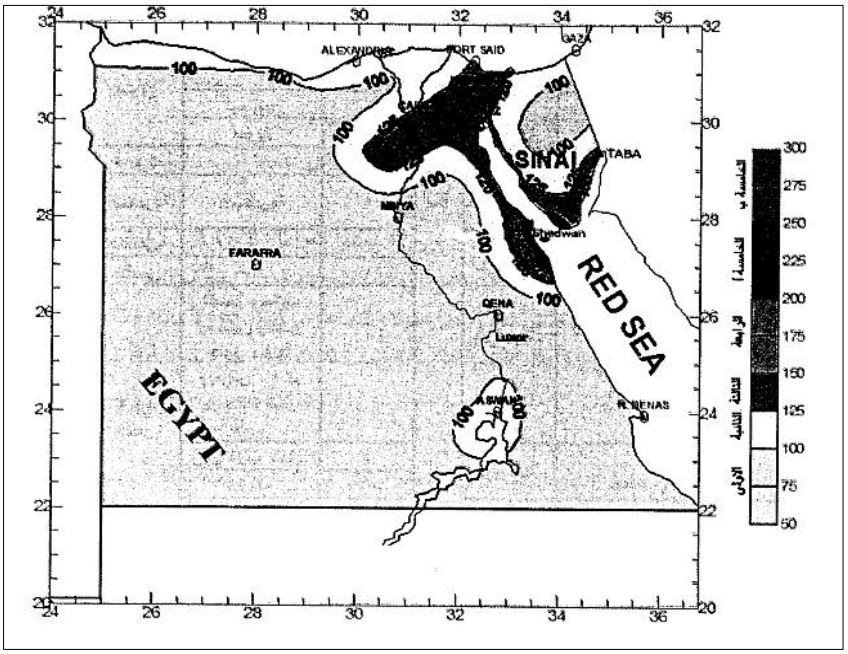

Figure 5. Earthquake Map in Egypt with the Location of Suez Canal Cable-Stayed Bridge (Zone 3) per ECP-201 (2012) [10]

In the context of seismic analysis, scaling of ground motion records is a critical step to ensure that the seismic inputs used in the analysis accurately reflect the expected seismic forces as defined by the Eurocode 8 parameters. Scaling involves adjusting the intensity of a recorded ground motion to match the target spectral acceleration at the structure's fundamental period T_1 . This is done by first calculating the spectral acceleration of the original ground motion at T_1 and then comparing it to the target spectral acceleration derived from the Eurocode 8 design spectrum. The scaling factor is determined by the ratio of the target spectral acceleration to the spectral acceleration of the original ground motion at T_1 . For example, if the target spectral acceleration at T_1 is higher than that of the original ground motion, the scaling factor will be greater than 1, meaning the entire ground motion record will be amplified. Conversely, if the target spectral acceleration is lower, the scaling factor will be less than 1 as shown in Table 4, resulting in a reduction in the ground motion intensity. Once the scaling factor is calculated, it is applied uniformly to the entire ground motion record, effectively adjusting the acceleration values throughout the time history to ensure that the structure's response under analysis is based on seismic inputs that are consistent with the specific seismic hazard and soil conditions outlined by the Eurocode 8 standards. In this study, while Eurocode 8 parameters are used for scaling, the Egyptian ECP-201 (2012) [10] design values, as illustrated in part of Table 3 as per *ECP 201-2012 Tabel (8-2-B): Seismic Effect Zones for Selected Egyptian Cities (Cairo, Giza, North Sinai, South Sinai)*, are adopted to remain consistent with local code requirements and prevailing engineering practice. Although updated seismic hazard maps may exist, ECP-201 (2012) [10] remains

the official national reference for seismic design in Egypt, and its use ensures compliance with current regulations. This process is essential to achieving a realistic and code-compliant seismic design that ensures the structure can withstand the seismic demands expected at the site.

Table 4. Scaling Factors for Response Spectrum

	Response Spectrum	Scale factor		Response Spectrum	Scale factor
1	5082-235	0.914934981	16	H-EDA270	0.388886201
2	A-CAM009	13.10752346	17	HWA011-E	1.425351416
3	ADL250	1.681130074	18	HWA013-E	0.603011643
4	BRA225	1.679897122	19	IND000	12.97756218
5	CCN090	9.894340066	20	JEN022	0.198242181
6	CHY025-N	1.188347458	21	LCN260	0.383402055
7	CHY029-N	1.394332507	22	LDM064	0.647502396
8	CHY036-N	2.07101241	23	PET000	3.939019304
9	CHY046-N	1.698898368	24	PMN000	12.44858546
10	CHY080-N	3.58456921	25	PUL164	0.783157441
11	D-PVP270	1.874802313	26	SCE018	0.242308233
12	ERZ-NS	0.258336404	27	TAP007-S	1.498553958
13	G04000	0.341298525	28	TCU089-E	0.883951655
14	H-E05140	0.341298525	29	TCU112-E	0.406827357
15	H-E12140	1.207294624	30	TCU141-N	0.53604955

6.1. Elastic Response Spectrum Equations with Subscripts and Superscripts

The following equations are for the Elastic Response Spectrum with proper formatting for subscripts and superscripts (Figure 6):

$$0 \le T \le T_B \quad S_c(T) = a_g.S.\left[1 + \frac{T}{T_B}.(\eta.\beta_0 - 1)\right] \tag{2}$$

$$T_B \le T \le T_c \quad S_c(T) = a_g.S.\eta.\beta_0 \tag{3}$$

$$T_C \le T \le T_D \quad S_c(T) = a_g.S.\eta.\beta_0.\left[\frac{T_C}{T}\right]^{K_1} \tag{4}$$

$$T_D \le T \quad S_c(T) = a_g.S.\eta.\beta_0.\left[\frac{T_C}{T_D}\right]^{K_1}.\left[\frac{T_D}{T}\right]^{K_2} \tag{5}$$

where: Soil Type (B); a_g =0.15g; S =1.35; η =1.0; β_0 =2.5; K_1 =1.0; K_2 =2.0; T_B =0.05; T_c =0.25; T_d =1.2.

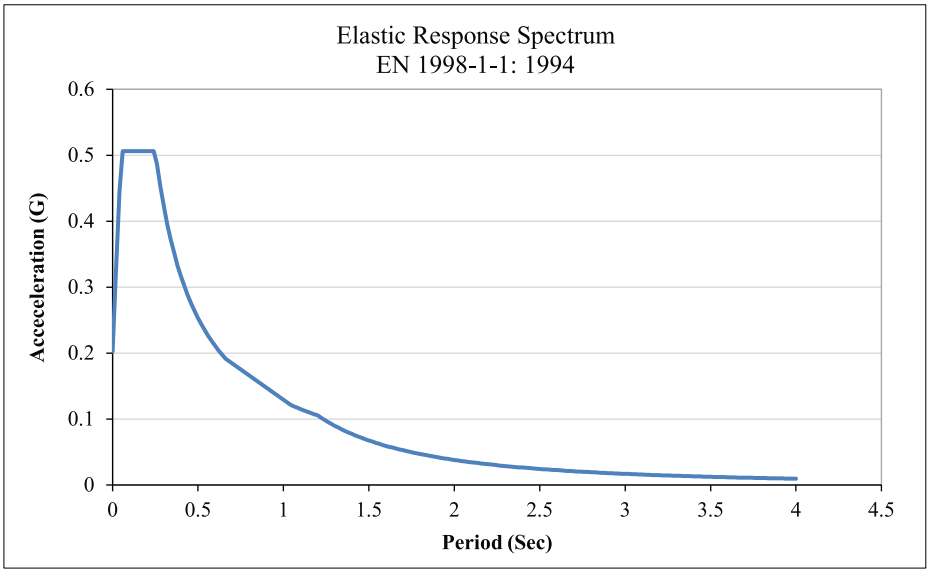

Figure 6. Elastic Response Spectrum

7. Pushover Analysis for Structural Performance Evaluation

The pushover analysis of a cable-stayed bridge, which stands 154 meters tall, demonstrates how the structure responds to increasing lateral forces, such as seismic or wind forces in Table 5. The horizontal axis represents the displacement in millimeters. Under applied forces, while the vertical axis represents the base shear in KN, as illustrated in Table 3 which reflects the total lateral force resisted by the structure. Initially, the bridge behaves elastically, where the base shear increases proportionally with the displacement. As the load increases, the bridge moves into a plastic phase, where deformations become larger without a significant increase in base shear. Eventually, the structure reaches its maximum capacity, and beyond this point, the base shear may decrease, indicating failure or collapse.

Table 5. Relationship between Displacement and Base Shear in Pushover Analysis

Step	Monitored Displacement (mm)	Base Force (kN)
0	0	0
1	500	11569.504
2	1000	13737.0528
3	1500	14893.1212
4	2000	15192.1149
5	2500	16039.9324
6	3000	15724.1925
7	3500	16043.6137
8	4000	17344.1995
9	4500	17675.0727
10	5000	13586.7097

At the start of the curve, the base shear increases steeply as the displacement remains small, representing the elastic behavior where the bridge resists lateral forces without permanent deformation. The point where the structure transitions from elastic to inelastic behavior is referred to as immediate occupancy. Although some components may have yielded, the overall structural integrity remains intact, and the bridge is still functional.

As the lateral load increases further, the curve begins to flatten, marking the plastic phase. In this region, deformations become larger and permanent, even though the structure continues to resist increasing forces. This point is known as life safety, where the structure protects lives but may require significant repairs to remain functional.

The peak of the curve occurs around 4000 millimeters of displacement, representing the maximum base shear the structure can handle (in Figure 7). Beyond this point, the base shear begins to decline, indicating that critical components, such as cables or the tower, are starting to fail. This phase is associated with collapse prevention, where the structure is at risk of collapse and can no longer safely carry additional loads.

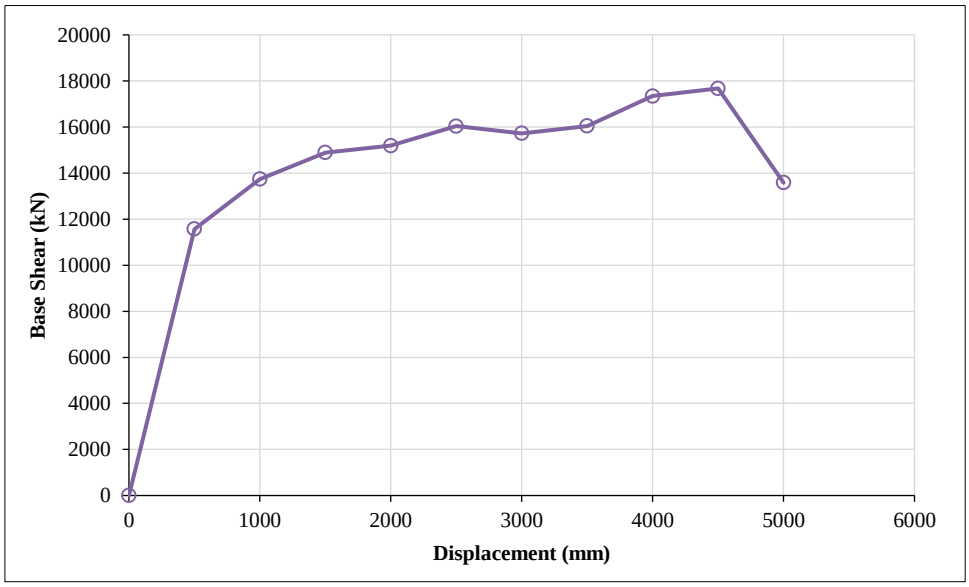

Figure 7. Pushover Curve at the longitudinal direction

These performance points, immediate occupancy, life safety, and collapse prevention, are critical for understanding the bridge's behavior under extreme conditions. Immediate occupancy reflects the structure's ability to remain functional after moderate damage. Life safety ensures the protection of lives, although the bridge would require repairs. Collapse prevention marks the stage where the structure is on the verge of collapse, with significant structural damage.

By identifying these key points, engineers can design and reinforce the bridge to better withstand lateral forces, ensuring its safety and resilience under extreme loading conditions.

8. Fragility Analysis

Sa(T1) as the intensity measure (IM), provides a probabilistic assessment of the seismic vulnerability of the cable-stayed tower. Four performance states were considered: Operational (OP), Immediate Occupancy (IO), Damage Control (DC), and Collapse Prevention (CP). The curves were developed using lognormal fragility functions, calibrated from performance point data obtained through pushover analysis (Figure 8).

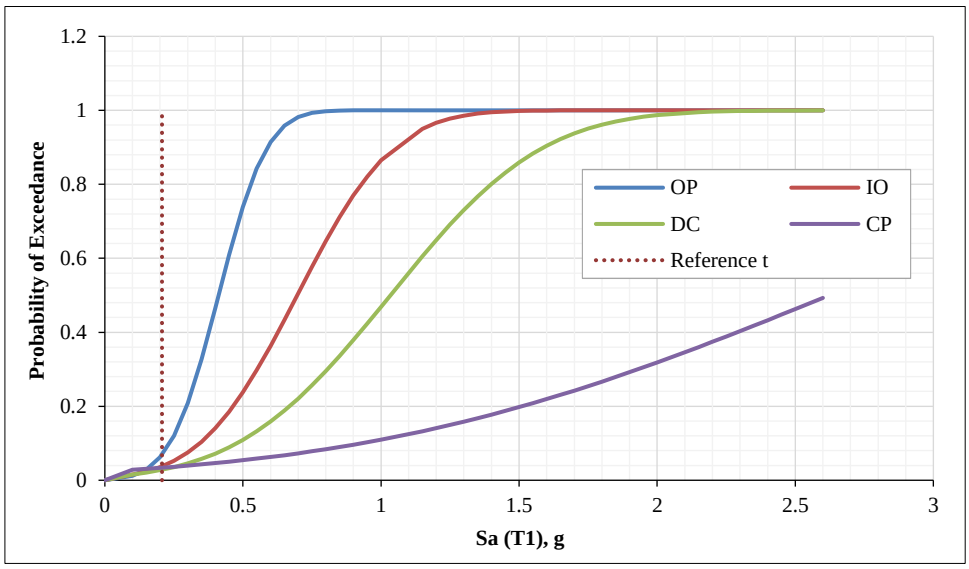

Figure 8. Fragility Curve for Displacement of Tower at the top

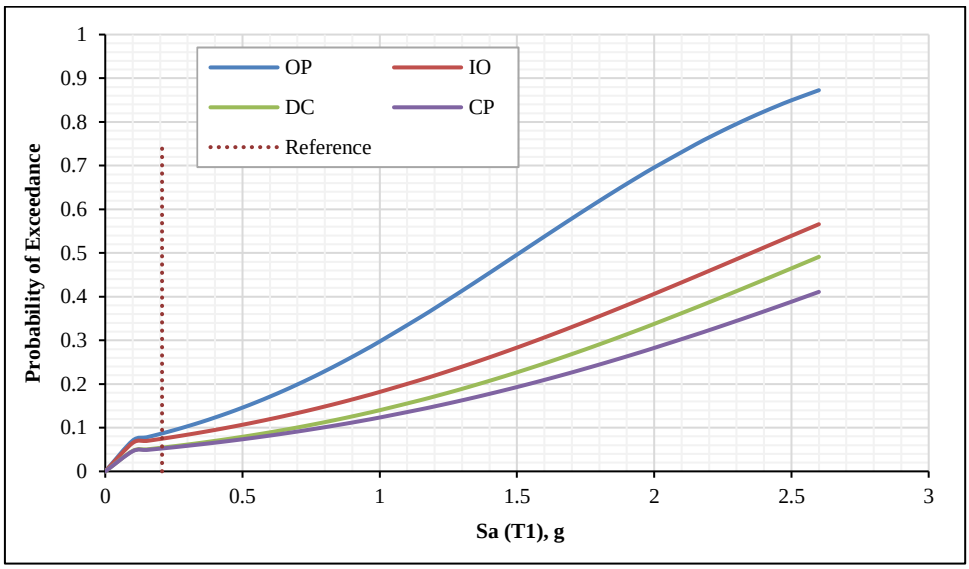

Figure 9. Fragility curve for moment of tower at the middle with girder of bridge

At the reference Sa(T1) = 0.207 g, corresponding to the OP performance point in Figure 8, the probability of exceeding OP is ~62%, while IO, DC, and CP remain below 4%. As seismic intensity increases, exceedance probabilities rise sharply. At 0.5 g, OP reaches 74%, IO 23.8%, DC 10.9%, and CP 5.4%. At 1.0 g, OP is almost certain (>99.9%), IO approaches 86.5%, DC exceeds 46.9%, and CP 10.9%. Under extreme shaking (2.0 g), DC exceedance surpasses 98% and CP exceeds 31%, indicating critical near-collapse conditions. These results highlight the bridge's limited ductility beyond the IO state and steep vulnerability gradient under high-intensity events.

Additionally, the fragility curve for the tower–girder moment demand (Figure 9) shows that this connection is highly sensitive, with significant exceedance probabilities even at moderate shaking (Sa ≈ 0.2 g). At higher intensities, the exceedance of severe states increases more rapidly than in the global tower displacement curves, emphasizing the critical role of the tower–girder interface in overall system performance.

It is also important to acknowledge that fragility curve results may vary if a different set of ground motions were employed, particularly those derived from more recent seismic events. Since the selection and scaling of input motions directly influence the dispersion and median capacity estimates, using updated ground motion records could shift the probability estimates of exceeding specific limit states. This reinforces the need for continuous refinement of fragility analyses as more representative seismic data become available.

In summary, Figures 8 and 9 demonstrate that while the bridge retains acceptable functionality under moderate shaking, both global tower displacements and local tower–girder moments exhibit rapid deterioration beyond the IO state. This underscores the need for targeted retrofitting, particularly at the tower–girder interface, to delay the onset of severe and collapse-prevention states.

9. The Monte Carlo Method for Analyzing Fragility Curves

In seismic fragility analysis, Monte Carlo simulation is a reliable probabilistic method for modeling complexity and uncertainty. Monte Carlo simulation was created in this work using Python for the following damage states: Operational Phase (OP), Immediate Occupancy (IO), Damage Control (DC), and Collapse Prevention (CP). These simulations ensured an accurate depiction of structural performance under seismic loads by taking into account uncertainties in geometry, material properties, and seismic inputs by using the data (Table 6).

Table 6. Mean and Standard Deviation Extracted from Fragility Curves

Phase	Mean	STDEV
Operational phase (OP)	0.341183	0.13767
Immediate occupancy (IO)	0.696502	0.27535
Damage Control (DC)	1.033709	0.433851
Collapse Prevention (CP)	2.623605	1.322335

Sample size has a significant effect on Monte Carlo simulation, influencing both the precision and reliability of the results. Smaller sample sizes (e.g., 100) fail to adequately represent the variability of input parameters, leading to noisy and irregular distributions. As a result, the outcomes may become unreliable and fail to reflect the true probabilistic behavior of the system [25]. The Monte Carlo simulation uses the following equation:

$$X_i = e^{\mu+\sigma Z_i} \tag{6}$$

where X_i Represents the simulated structural response or parameter for the i-th sample. This is the value generated for a specific simulation instance based on the lognormal distribution, and μ is the mean of the natural logarithm (ln) of the variable in the lognormal distribution. It is calculated as:

$$\mu = \ln(M) - 0.5\sigma^2 \tag{7}$$

here, M is the mean of the variable in its original (non-logarithmic) scale; σ is the standard deviation of the natural logarithm (ln) of the variable in the lognormal distribution, and Z_i A standard normal random variable, which means: $Z_i \sim N(0,1)$.

This represents a random value drawn from a normal distribution when using equation 6 with a mean of 0 and a standard deviation of 1 [26]. The probabilistic variability of the structural response to seismic loads is shown by the Monte Carlo simulation distributions for each damage condition (OP, IO, DC, and CP). With a lengthy tail toward higher values, these histograms which are produced using lognormal distributions showcase (in Figure 10 to 12) the potential for extreme situations while highlighting how values are clustered around their respective means. Minor damage occurs at lower earthquake intensities, as indicated by the Operational Phase (OP) values, which are centered around a lower mean (~0.34). The necessity for moderate seismic intensity is reflected in the shift in Immediate Occupancy (IO), which has a slightly higher mean (~0.69). For Collapse Prevention (CP) and Damage Control (DC) as illustrated in Table 3, the distributions shift to much higher means (~2.62 and ~1.03, respectively). Variyavwala et al. [13] signifying the increased intensity levels needed for these degrees of severe damage. At higher damage levels, there is more uncertainty in the structural response, as indicated by the broader spread in these distributions. The tails of these distributions show the tiny but significant likelihood that extreme seismic occurrences will have catastrophic consequences, especially for DC and CP. These distributions highlight the significance of taking uncertainties into account in seismic design and risk assessment, and they offer insightful information on the probabilistic behavior of the structure [27, 28].

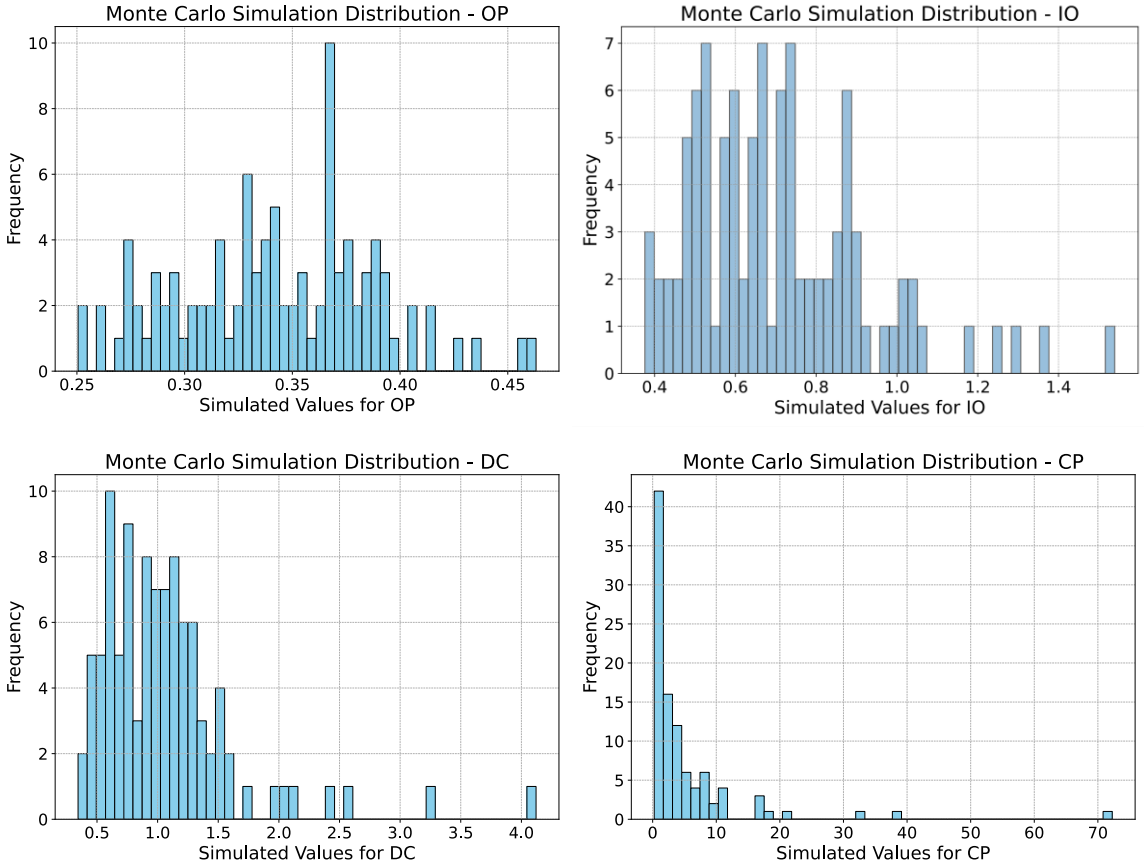

Figure 10. Monte Carlo Simulation Results-100 Simulation

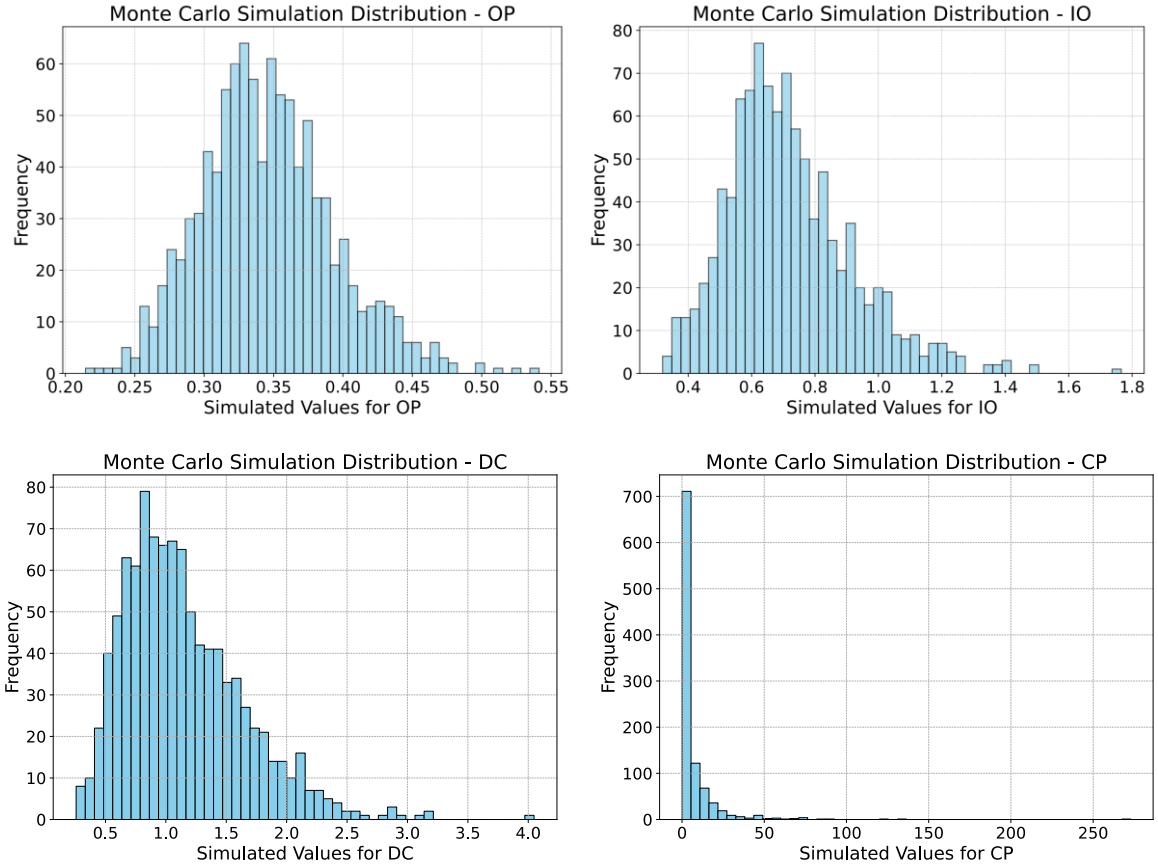

Figure 11. Monte Carlo Simulation Results-1000 Simulation

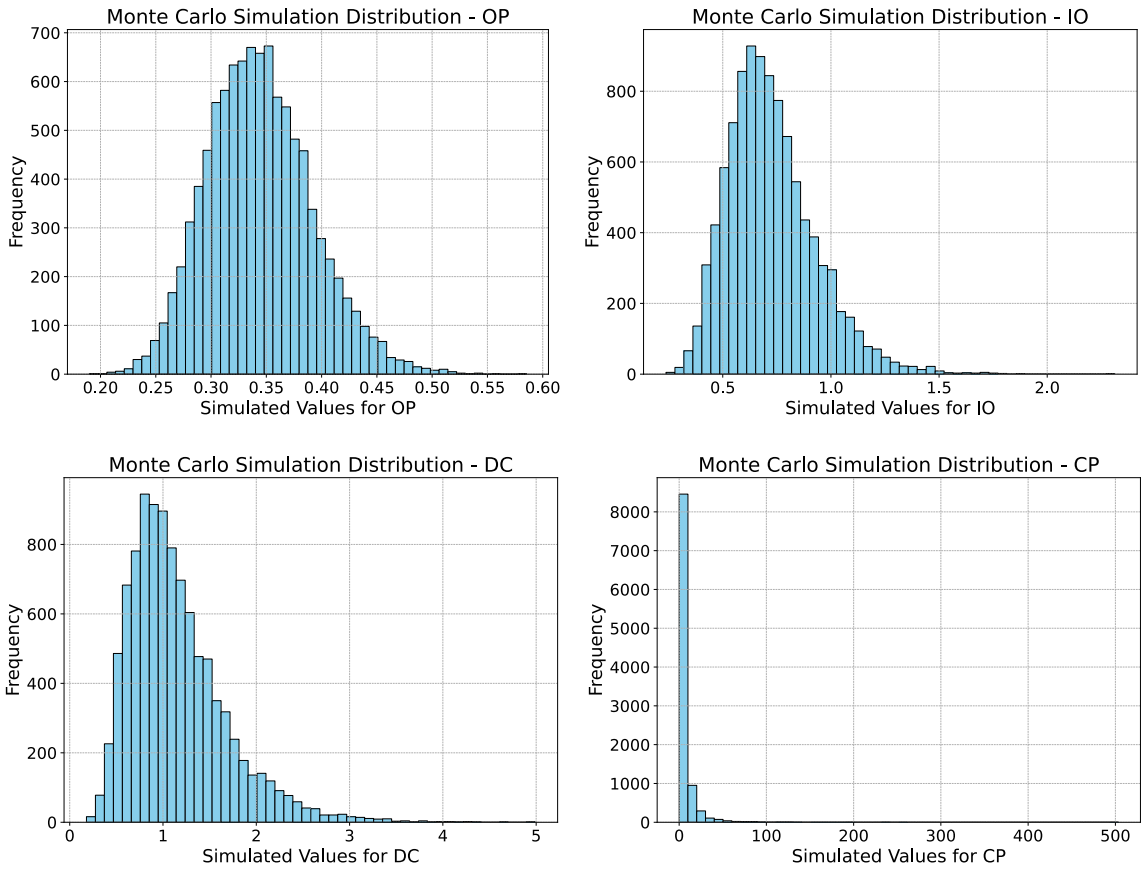

Figure 12. Monte Carlo Simulation Results-10000 Simulation

Monte Carlo simulation distributions were compared for three sample sizes (100, 1000, and 10,000 simulations). The findings show how the generated distributions for each damage state (OP, IO, DC, and CP) are affected by sample size in terms of consistency and smoothness. While smaller samples, such as 100 simulations, exhibit noticeable unpredictability and chaotic patterns, larger samples, such as 10,000 simulations, yield more stable and smooth distributions. This stability indicates that statistical convergence is reached with rising sample counts.

The probabilistic variability of the structural response to seismic loads is shown by the Monte Carlo simulation distributions for each damage condition (OP, IO, DC, and CP). With a lengthy tail toward higher values, these histograms which are produced using lognormal distributions—showcase the potential for extreme situations while highlighting how values are clustered around their respective means. Minor damage occurs at lower earthquake intensities, as indicated by the Operational Phase (OP) values, which have a mean of 0.345171, a standard deviation of 0.048081, and a 5%–95% quantile range of 0.272382–0.429998. The necessity for moderate seismic intensity is reflected in the shift in Immediate Occupancy (IO), which has a mean of 0.723996, a standard deviation of 0.203490, and a quantile range of 0.446685–1.097801. For more severe states, the distributions shift to much higher means: Damage Control (DC) records a mean of 1.130754, a standard deviation of 0.511776, and a quantile range of 0.506758–2.082571, while Collapse Prevention (CP) shows a mean of 6.411419, a standard deviation of 13.695909, and a wide quantile range of 0.278969–23.3 (Table 7). At higher damage levels, there is more uncertainty in the structural response, as indicated by the broader spread in these distributions. The tails of these distributions show the tiny but significant likelihood that extreme seismic occurrences will have catastrophic consequences, especially for DC and CP. These distributions highlight the significance of taking uncertainties into account in seismic design and risk assessment, and they offer insightful information on the probabilistic behavior of the structure.

Table 7. Statistical parameters for different damage states

Damage	State	Mean	Std. Dev.	5% Quantile	95% Quantile
0	OP	0.345171	0.048081	0.272382	0.429998
1	IO	0.723996	0.20349	0.446685	1.097801
2	DC	1.130754	0.511776	0.506758	2.082571
3	CP	6.411419	13.69591	0.278969	23.3

The Monte Carlo simulation results indeed indicate significant uncertainty in the Collapse Prevention (CP) and Damage Control (DC) states, which reflects the variability in structural performance under high seismic demands. In real projects, this uncertainty can be mitigated through several practical measures. First, conducting detailed site-specific seismic hazard assessments can reduce variability in input ground motions. Second, implementing rigorous structural health monitoring and inspection programs enables the identification and repair of vulnerabilities before major seismic events. Third, applying performance-based seismic design with enhanced safety factors for critical components can provide additional robustness. Furthermore, advanced material characterization and quality control during construction can help minimize deviations from design assumptions. Finally, retrofitting strategies such as base isolation, energy dissipation devices, and strengthening of key load-carrying members can reduce the likelihood of severe damage, thereby lowering the spread of possible responses in these high-damage states.

10. Discussion

10.1. Strategic Significance and Seismic Context

The Salam Bridge is a critical structural link between the Sinai Peninsula and Egypt's national transportation network, making its seismic resilience a priority for both safety and economic stability, due to its long-span cable-supported configuration and strategic location, the bridge is susceptible to seismic hazards that can compromise serviceability and structural integrity, recent literature has shown that large-span bridges, especially those with cable-stayed or suspension systems, exhibit heightened sensitivity to dynamic loading due to their flexible nature and complex modal interactions, this reinforces the need for a targeted seismic vulnerability analysis specific to the Salam Bridge's geometry and load distribution.

10.2. Structural Behavior from Pushover Analysis

Pushover analysis shows a base shear capacity of approximately 18 000 kN, an ultimate displacement around 5 m, and instability inception near 4000 mm, indicating a narrow nonlinear-to-collapse margin, consistent with behavior observed in large cable-stayed structures under monotonic overload [29]. Fragility curve analysis yields increasing median spectral accelerations across damage states: OP = 0.345 g ($\sigma \approx 0.048$ g), IO = 0.724 g ($\sigma \approx 0.203$ g), DC = 1.131 g ($\sigma \approx 0.512$ g), and CP = 6.411 g ($\sigma \approx 13.696$ g), wherein the escalating uncertainty at CP aligns with recent findings that highlight severe variability in high-demand fragility ranges for cable-stayed bridges [30].

10.3. Probabilistic Amplification and Monte Carlo Insights

Using Monte Carlo simulation, the probability of exceeding DC or CP rises sharply with increasing Sa(T1), reinforcing modern studies advocating integration of probabilistic sampling with capacity-based analysis to encapsulate demand and capacity uncertainties effectively [31], this multifaceted approach underscores that while the bridge performs reliably under low-to-moderate seismic demand, its vulnerability grows rapidly near DC–CP performance states.

10.4. Comparison with Contemporary Seismic Fragility Studies

Comparative analysis shows alignment with frameworks where multi-support and non-Gaussian ground motion characteristics significantly influence system fragility and resilience [32], and life-cycle fragility assessments reveal that time-dependent deterioration substantially affects damage probabilities of key components [33]. The Salam Bridge analysis corroborates these observations, as component vulnerability particularly CP susceptibility is notably sensitive to both modelling uncertainty and seismic intensity escalation. This integrated methodology, combining pushover analysis, fragility curves, and Monte Carlo uncertainty quantification, provides a strong foundation for developing retrofit strategies. In this context, retrofitting measures are prioritized by implementing low-cost, high-impact interventions first, followed by more resource-intensive but life-safety–critical actions, ensuring both cost-effectiveness and effective seismic risk reduction [34, 35]. Such a tiered approach enables resource-efficient resilience interventions for vital infrastructure like Salam Bridge, particularly near DC and CP thresholds

11. Conclusion

Bridge's main tower highlights a robust correlation between probabilistic seismic demand and structural vulnerability. The Monte Carlo outputs, with mean values of 0.341 (OP), 0.697 (IO), 1.034 (DC), and 2.624 (CP) and respective standard deviations of 0.138, 0.275, 0.434, and 1.322, reveal that at low seismic intensities, structural responses remain tightly clustered around the OP and IO thresholds. This behavior implies minimal damage risk, steady performance, and adequate serviceability under minor seismic events. As seismic intensity escalates, however, the distribution of simulated values becomes significantly wider, intersecting the DC and CP thresholds with increasing frequency. This spread indicates a progressive rise in vulnerability, where the main tower experiences more severe responses. The widening uncertainty bands at high intensities especially around the DC and CP states suggest a higher probability of sudden structural failure when subjected to strong ground motions. These trends closely align with the fragility curves, which exhibit a sharp increase in the probability of exceeding DC and CP states once moderate to high seismic demands are reached.

Integrating these insights makes it evident that the El Salam Bridge's current design leaves it susceptible to significant collapse risks in severe earthquakes, as it was not originally engineered to endure high-magnitude seismic forces. Even moderate earthquakes could cause minor yet cumulative damage, gradually undermining long-term stability and operational safety. Structural weak points are concentrated at the base connections and cable anchorage systems, where stress concentrations are most critical under dynamic loading. Without mitigation, these vulnerabilities could escalate the likelihood of functional loss or collapse in a major seismic event. Therefore, targeted retrofitting measures—such as the incorporation of high-strength materials, additional seismic bracing, and advanced real-time structural health monitoring are essential. These interventions would enhance the bridge's resilience against sudden extreme loads and enable early detection of damage progression, supporting timely maintenance. By combining Monte Carlo simulations with fragility-based probabilistic evaluation, stakeholders can adopt a risk-informed strategy to prioritize interventions and secure the bridge's role as a resilient, reliable link in Egypt's transportation network.

12. Nomenclature

PGA	Peak Ground Acceleration	Sa(T1)	Spectral Acceleration at Fundamental Period
IM	Intensity Measure	CDF	Cumulative Distribution Function
OP	Operational	IO	Immediate Occupancy
DC	Damage Control	CP	Collapse Prevention
ECP	Egyptian Code of Practice	MC	Monte Carlo
LS	Limit State		

13. Declarations

13.1. Author Contributions

Conceptualization, N.M. and W.A.A.; methodology, N.M.; software, N.M.; validation, W.A.A. and M.S.E.; formal analysis, N.M.; data curation, N.M.; writing—original draft preparation, N.M.; writing—review and editing, W.A.A. and M.S.E.; supervision, W.A.A. and M.S.E. All authors have read and agreed to the published version of the manuscript.

13.2. Data Availability Statement

The data presented in this study are available in the article.

13.3. Funding

The authors received no financial support for the research, authorship, and/or publication of this article.

13.4. Conflicts of Interest

The authors declare no conflict of interest.

14. References

[1] Nazmy, A. S., & Abdel-Ghaffar, A. M. (1990). Non-linear earthquake-response analysis of long-span cable-stayed bridges: Theory. Earthquake Engineering & Structural Dynamics, 19(1), 45-62. doi:10.1002/eqe.4290190106.

[2] Abdel- Ghaffar, A. M., & Nazmy, A. S. (1991). 3D Nonlinear Seismic Behavior of Cable-Stayed Bridges. Journal of Structural Engineering, 117(11), 3456–3476. doi:10.1061/(asce)0733-9445(1991)117:11(3456).

[3] Shinozuka, M., Feng, M. Q., Lee, J., & Naganuma, T. (2000). Statistical Analysis of Fragility Curves. Journal of Engineering Mechanics, 126(12), 1224–1231. doi:10.1061/(asce)0733-9399(2000)126:12(1224).

[4] Kim, S. H., & Shinozuka, M. (2004). Development of fragility curves of bridges retrofitted by column jacketing. Probabilistic Engineering Mechanics, 19(1), 105–112. doi:10.1016/j.probengmech.2003.11.009.

[5] Li, L., Hu, S., & Wang, L. (2017). Seismic fragility assessment of a multi-span cable-stayed bridge with tall piers. Bulletin of Earthquake Engineering, 15(9), 3727–3745. doi:10.1007/s10518-017-0106-x.

[6] Chen, C., Liu, J., Lin, J., & Li, S. (2024). Seismic fragility analysis of three-tower cable-stayed bridges with different connection configurations. Earthquake Engineering and Engineering Vibration, 23(4), 1009–1027. doi:10.1007/s11803-024-2285-1.

[7] Liang, Y., Zhao, T., Wei, Y., & Guan, P. (2025). Fragility analysis of cross-sea highway cable-stayed bridges under seismic-wind combined loading. Engineering Failure Analysis, 173, 109451. doi:10.1016/j.engfailanal.2025.109451.

[8] Li, C., Li, H. N., Hao, H., Bi, K., & Chen, B. (2018). Seismic fragility analyses of sea-crossing cable-stayed bridges subjected to multi-support ground motions on offshore sites. Engineering Structures, 165, 441–456. doi:10.1016/j.engstruct.2018.03.066.

[9] Guo, J., Gu, Y., Wu, W., Chu, S., & Dang, X. (2022). Seismic Fragility Assessment of Cable-Stayed Bridges Crossing Fault Rupture Zones. Buildings, 12(7), 1045. doi:10.3390/buildings12071045.

[10] ECP-201. (2012). Egyptian Code for Calculation of. Loads and Forces for Buildings. Research center for housing and building, Giza, Egypt.

[11] Tang, H., Xu, W., & Yi, J. (2024). Seismic performance of cable-stayed bridges under large earthquake ground motions considering the loss of stay cables. Case Studies in Construction Materials, 20, 2888. doi:10.1016/j.cscm.2024.e02888.

[12] Pang, Y., Wu, X., Shen, G., & Yuan, W. (2014). Seismic Fragility Analysis of Cable-Stayed Bridges Considering Different Sources of Uncertainties. Journal of Bridge Engineering, 19(4), 4013015. doi:10.1061/(asce)be.1943-5592.0000565.

[13] Variyavwala, J. P., Gondaliya, K. M., Desai, A. K., & Noroozinejad Farsangi, E. (2023). Seismic fragility estimation of cable-stayed bridges with various pylon shapes considering soil-pile interaction. Bulletin of Earthquake Engineering, 21(7), 3647–3671. doi:10.1007/s10518-023-01647-5.

[14] Seleemah, M. A., Helam, M. S., Abu-alenein, M. A., Hammad, E. B., Goda, M. S., Seleemah, A. A., & Elkady, A. Z. (2022). Response of Aswan cable-stayed bridge to spatial non-synchronous seismic excitations. Journal of Engineering and Applied Science, 69(1), 70. doi:10.1186/s44147-022-00124-1.

[15] Jia, Y., Xin, L., Yang, D., Pei, M., Zhao, L., & Huang, Z. (2024). Seismic behavior analysis of long-span cable-stayed bridge under bi-directional near-fault ground motions. Structures, 64. doi:10.1016/j.istruc.2024.106512.

[16] Hosseinpour, F., & Abdelnaby, A. E. (2017). Fragility curves for RC frames under multiple earthquakes. Soil Dynamics and Earthquake Engineering, 98, 222–234. doi:10.1016/j.soildyn.2017.04.013.

[17] Karim, K. R., & Yamazaki, F. (2003). A simplified method of constructing fragility curves for highway bridges. Earthquake Engineering & Structural Dynamics, 32(10), 1603–1626. doi:10.1002/eqe.291.

[18] Shinozuka, M., Feng, M. Q., Kim, H.-K., & Kim, S.-H. (2000). Nonlinear Static Procedure for Fragility Curve Development. Journal of Engineering Mechanics, 126(12), 1287–1295. doi:10.1061/(asce)0733-9399(2000)126:12(1287).

[19] Vosooghi, A., & Saiidi, M. S. (2012). Experimental fragility curves for seismic response of reinforced concrete bridge columns. ACI Structural Journal, 109(6), 825–834. doi:10.14359/51684126.

[20] Sangadji, S., Wibowo, N. A., Tropormera, E. N., Purwanto, E., & Kristiawan, S. A. (2017). Fragility function for assessing seismic risk of typical concrete bridge by means of nonlinear static and dynamic analysis. MATEC Web of Conferences, 138, 2005. doi:10.1051/matecconf/201713802005.

[21] Varga, S., & Chiorean, C. G. (2016). Seismic Assessment of Reinforced Concrete Frameworks through Advanced Pushover Analysis and Nonlinear Response of a SDOF Oscillator. Procedia Engineering, 161, 332–336. doi:10.1016/j.proeng.2016.08.568.

[22] Abou-Rayan, A. M. (2002). Three-Dimensional Nonlinear Seismic Behavior of Suez-Canal Cable-Stayed Bridge. Proceedings of the 4th International Conference on Civil and Architecture Engineering, Military Technical College, 14-16 May, 2002, Cairo Egypt.

[23] Shahi, R., Lam, N. T., Gad, E. F., Saifullah, I., Wilson, J. L., & Watson, K. (2014). Choice of intensity measure in incremental dynamic analysis. Proceedings of the Australian Earthquake Engineering Society 2014 Conference, 21-23 November, 2014, Lorne, Australian.

[24] Farag, M. M. N., Mehanny, S. S. F., & Bakhoum, M. M. (2015). Establishing optimal gap size for precast beam bridges with a buffer-gap-elastomeric bearings system. Earthquake and Structures, 9(1), 195–219. doi:10.12989/eas.2015.9.1.195.

[25] Šiška, D. (2016). Monte Carlo Methods. Available online: https://webhomes.maths.ed.ac.uk/~dsiska/MonteCarloMethods.pdf (accessed on October 2025).

[26] Sarsoruo, C., Gebo, R., & Anderson, P. K. (2019). Simulating the lognormal distribution: A Monte Carlo method. Electronic Journal of Informatics, 1, 73-89. doi:10.1137/1012001.

[27] Shinozuka, M., & Deodatis, G. (1997). Effect of Spatial Variation of Ground Motion for Ordinary Bridges. Proceedings of the 7th US-Japan Workshop on Earthquake Disaster Prevention for Lifeline Systems, 4-7 November, 1997, Seattle, United States

[28] Halton, J. H. (1970). A retrospective and prospective survey of the Monte Carlo method. Siam Review, 12(1), 1-63.

[29] Jiao, C. Y., Li, J. Z., & Long, P. H. (2012). Seismic fragility analysis of long-span cable-stayed bridges. Advanced Science Letters, 12(1), 160-164. doi:10.1166/asl.2012.2830.

[30] Liang, Y., Kong, Y., Yan, L., Zhao, Z., & Guan, P. (2025). Multi-hazard fragility analysis of cross-sea cable-stayed bridges cable bent tower under seismic-wind combined action. Soil Dynamics and Earthquake Engineering, 195, 109422. doi:10.1016/j.soildyn.2025.109422.

[31] Jiang, H., Bai, X., Song, G., Wang, L., Zeng, C., Xue, Z., & Zhao, X. (2024). Fragility assessment of sea-crossing cable-stayed bridge subjected to multi-hazard action via TKC and R-vine copula. Engineering Structures, 307, 117874. doi:10.1016/j.engstruct.2024.117874.

[32] Lan, Y., Xu, J., Zhong, J., & Li, Y. (2024). Seismic fragility and resilience assessment of large-span cable-stayed bridges under multi-support ground motions with non-Gaussian characteristics. Earthquake Engineering & Structural Dynamics. doi:10.1002/eqe.4220.

[33] Lu, X., Wei, K., He, H., & Qin, S. (2022). Life-cycle seismic fragility of a cable-stayed bridge considering chloride-induced corrosion. Earthquake Engineering and Resilience, 1(1), 60–72. doi:10.1002/eer2.7.

[34] FEMA 547. (2006). (Techniques for the seismic rehabilitation of existing buildings (FEMA 547). Federal Emergency Management Agency (FEMA), Washington, United States.

[35] EN 1998-3. (2005). Eurocode 8, Design of Structures for Earthquake Resistance, Part 3: Assessment and Retrofitting of Buildings. European Committee for Standardization (CEN), Brussels, Belgium.